ACS Sustainable Chemistry & Engineering

pubs.acs.org/journal/ascecg

Research Article

Engineering Tunable Biomimetic Superhydrophobic Surfaces from Natural Spiky Pollen

Jian Li,[†] Chenchen Zhou,[†] Jun Hao Mo,[†] Ruiyan Ni, Jiwon Lee, Chee Hao Teo, Zi Hao Guo, Hanna Kim, Mohammed Shahrudin bin Ibrahim, Bernard P. Binks, and Nam-Joon Cho*

Cite This: *ACS Sustain. Chem. Eng.* 2026, 14, 14720−14732

Read Online

ACCESS | Metrics & More | Article Recommendations | Supporting Information

ABSTRACT: Superhydrophobic surfaces are essential to a wide range of applications from self-cleaning and anti-icing surfaces on aircraft to antifouling coatings on maritime vessels. However, most artificial superhydrophobic surface designs rely heavily on fluorinated materials, raising serious environmental concerns due to their bioaccumulation and potential carcinogenicity. Natural spiky pollen, an underutilized biowaste, offers a promising alternative to fluorine-based approaches. These particles intrinsically possess a distinctive topography that closely mirrors the hierarchical superhydrophobic micro/nanostructures. Notably, their distinctive geometrical features can further influence and modulate surface wetting behavior. Here, we demonstrate the engineering of superhydrophobic surfaces using spiky pollen from diverse plant species (ragweed, two chrysanthemum subspecies, and sunflower) to investigate the influence of geometrical features on the superhydrophobic performance and to benchmark their effectiveness against fluorinated-modified counterparts. The engineered pollen-based superhydrophobic surfaces demonstrate exceptional water contact angles and tunable wetting states, ranging from Cassie-impregnating states ("petal effect") for shorter spike lengths to Cassie−Baxter states ("lotus effect") for longer spikes. This work establishes a sustainable and facile strategy for engineering advanced superhydrophobic surfaces using natural microarchitectures.

KEYWORDS: *superhydrophobic surfaces, pollen, sustainability, Cassie−Baxter, Cassie-impregnating*

INTRODUCTION

For thousands of years, natural organisms have evolved to possess superhydrophobic surface (SS) properties essential for their adaptation in diverse environmental conditions. A compelling example is the compound eyes of mosquitoes that possess ideal superhydrophobic and antifogging properties allowing them to maintain clear vision in a humid habitat.[1,2] Beyond mosquitoes, other natural organisms such as lotus leaves, rose petals, butterfly wings, and gecko feet have served as inspiration for the development of synthetic SSs that stay dry, self-clean, and resist biofouling.[3−5] These unique properties have facilitated their practical applications across various fields, including self-cleaning glass,[5] anti-icing coatings for aircraft,[6] drug delivery devices,[7] multifaceted coatings used for construction,[8] and antifouling coatings for maritime vessels.[9]

SSs are typically defined by a water contact angle (θ_{WCA}) exceeding 150° and a water sliding angle (θ_{WSA}) and contact angle hysteresis (θ_{CAH}) below 10°.[10−13] These characteristics arise from the synergistic combination of the hierarchical micro/nanostructured surface topographies and the material's low surface energy.[14,15] Lotus leaves and rose petals are classic examples of SS, with distinctive differences in their water adhesion behavior.[16,17] Water adhesion behavior can be evaluated via θ_{CAH}, with a highly adhesive surface possessing a $\theta_{CAH} > 100°$ and a low adhesive surface exhibiting a $\theta_{CAH} < 31°$. For reference, lotus leaves and rose petals display θ_{CAH} values of less than 5° and ∼76°, respectively.[13,16,17] Water droplets on lotus leaves easily roll off ("lotus effect") due to the manifestation of the Cassie−Baxter (CB) wetting state, in which air pockets trapped within the micro/nanostructures suppress droplet adhesion.[18−20] In contrast, droplets on rose petals are firmly adhered even when inverted ("petal effects") owing to their partial droplet inlaying into the surface resulting in the Cassie-Impregnating (CI) state.[21−23]

The development of bioinspired SS necessitates the establishment of hierarchical surface texture and minimized surface energy.[12,14,15] Among them, roughness is generally considered

Received: April 7, 2026
Revised: July 3, 2026
Accepted: July 6, 2026
Published: August 7, 2026

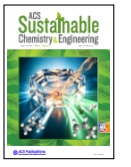

the more crucial component, as when the surface is roughened, both moderately hydrophobic and superhydrophobic surfaces can manifest similar wetting properties. Roughness enhancement of a surface can be achieved through techniques including lithography, etching, deposition, casting, and so forth.[12,24] In comparison, surface energy minimization is typically achieved through the application of low-surface-energy materials, including fluorinated silanes, organic silanes, fluorocarbons, and so forth. Present SS fabrication methods, such as sol−gel processing,[25,26] dip coating,[27,28] spray coating,[29,30] electrospinning,[31,32] and chemical vapor deposition,[33,34] are often expensive or environmentally detrimental, less efficient, complex, limited to small-scale substrates, and highly dependent on specialized and expensive equipment, restricting their application to laboratory settings. Moreover, the widely incorporated fluorinated materials pose toxic risks to the environment and living organisms when degraded. Therefore, it is essential to maintain high superhydrophobic properties while utilizing fluorine-free alternatives such as polydimethylsiloxane (PDMS), waxes, and alkylsilanes. This can be achieved by reducing the reliance on fluorinated materials or substituting with fluorine-free alternatives without compromising performance.[35]

Pollen is an inherently hydrophobic natural particle that exhibits species-dependent morphologies while maintaining relatively uniform size within the same species.[36,37] As an abundant, low-cost, renewable, and often underutilized biowaste, pollen represents a promising natural material for functional materials.[36,38] Notably, species with a spiky architecture resemble the micro/nanostructured surface characteristics of lotus leaves. Across the plant kingdom, numerous pollen species possess this spiky morphology, including ragweed, chrysanthemum, and sunflower, with variations in their size, spike length, and inter-spike spacing.[39,40] Inspired by lotus leaves, the inherently rough, spiky architecture of pollen supplies a ready-made micro/nanostructured template that when combined with low surface energy can yield a natural-derived sustainable SS. Critically, given the structural diversity of spiky pollen, these geometrical features may influence the wetting transitions and, consequently, contribute to variations in superhydrophobic performance, potentially reducing or eliminating the dependence on fluorinated modifications.

Here, we explore the potential of diverse spiky pollen species as natural building blocks for the fabrication of a pollen-based superhydrophobic surface (PSS), engineered with intrinsically low-surface-energy materials such as PDMS and 1*H*,1*H*,2*H*,2*H*-perfluorooctyl-trichlorosilane (FTS). The pollen's inherent morphologies were systematically evaluated for their superhydrophobic properties through θ_{WCA}, θ_{WSA}, and θ_{CAH} measurements, with direct comparisons drawn between PDMS and PDMS-FTS composite systems. Furthermore, pollen's geometrical features were assessed for their capacity to govern distinct wetting transitions through the formation of CB and CI wetting states. The PSS's durability and self-cleaning capabilities were subsequently evaluated to establish correlations between surface morphology, durability, wetting behavior, and functional performance, providing comprehensive insights into PSS's superhydrophobic performances. Collectively, this study transforms multifunctional pollen "biowaste" into a biomimetic SS, with promising applications in the field of self-cleaning coatings,[39] antifreezing coatings,[41] and biomedical applications,[42] among others. The transformation of pollen "biowaste" exemplifies a cross-economy approach moving beyond conventional circularity by converting low-value waste into high-value-added products.[38]

EXPERIMENTAL SECTION

Materials and Reagents

Raw bee pollen granules, including those from sunflower, wild chrysanthemum (C1 and C2), and ragweed, were sourced from Yuensun Biological Technology Co. Ltd. Diiodomethane (99%) for surface free energy characterization and FTS (97%) were procured from Sigma-Aldrich. A Sylgard 184 silicone elastomer kit or polydimethylsiloxane (PDMS) consisting of two components, a prepolymer (Part A) and a curing agent (Part B), with a default weight ratio of 10:1 was obtained from Dow Corning Corporation. Acetone (analytical reagent grade), diethyl ether (analytical reagent grade), and *n*-hexane were sourced from Thermo Fisher Scientific, RCI Labscan, and Tedia Company, respectively. All chemicals were used as received unless stated otherwise. A solid contaminant for self-cleaning applicability is natural river sand with particle sizes typically ranging from several micrometers to 2 mm. Nylon mesh was procured from Elko Filtering Co. LLC., and the abrasive paper (1000 CW) was purchased from Starcke.

Pollen Defatting

The defatting procedure of raw bee pollen followed the work previously described by Fan & Park et al.[37] Pollen granules (500 g) and deionized water (1 L) were stirred with a disperser (Eurostar 20 digital, IKA) for 2 h at 1000 rpm and 50 °C. The resulting pollen mixture was filtered using a 200 μm nylon mesh to remove any contaminants. Vacuum filtration was then employed to remove the excess water before redispersing it in acetone (1 L) for 3 h at 1000 rpm at room temperature (RT). Subsequently, the corresponding pollen residue underwent vacuum filtration to remove excess acetone and was continuously washed with acetone until the filtrate turned clear. The pollen powder was air dried in a fume hood for 12 h before mixing with 1 L of diethyl ether and stirring at 1000 rpm at RT for 2 h. The pollen powder was filtered, and the process was repeated twice with fresh diethyl ether. The pollen powder was redispersed in fresh diethyl ether and stirred overnight (12 h). The excess diethyl ether was removed through vacuum filtration, and the defatted pollen powder was dried overnight in the fume hood.

Pollen Superhydrophobic Surface (PSS) Fabrication

Defatted pollen (0.3 g), sourced from different species, was mixed with either PDMS or a PDMS-FTS mixture with a mass ratio of 3:7 to 7:3 for pollen to PDMS-FTS mixture and 8:2 for PDMS-FTS mixture alone, all added into a 4 mL glass vial. Upon adding *n*-hexane (2 mL), the vial was agitated for more than 5 min using a vortex (Vortex Genie 2) before casting the suspension uniformly on glass slides and leaving it to air dry in the fume hood. Finally, the dried coating was subsequently maintained at RT for >7 days to facilitate the complete curing of PDMS and FTS.

Imaging and Characterization

The morphologies and structures of pollen species and PSS were first analyzed using a field-emission scanning electron microscope (FE-SEM, JSM-7600F, Jeol). Subsequently, a contact angle meter (Attension Theta Flex C201, Biolin Scientific) was employed to measure θ_{WCA} of the PSS surface as well as θ_{CAH} and to evaluate the droplet adhesion capability through a bounce and adhesion test. The θ_{WCA} measurement was conducted at five random locations on the PSS, and θ_{CAH} was determined from the difference between the advancing and receding contact angles obtained by gradually increasing and withdrawing the volume of a 6 μL droplet. The bounce test was performed by releasing a 6 μL droplet from a height of approximately 6 mm above the PSS's surface. The droplet trajectory was extracted and analyzed using the ImageJ software. The droplet's total energy was estimated from its gravitational potential energy at the highest points both at release and after each bounce. The adhesion test was also conducted using a contact angle meter, with the droplet behavior monitored during

https://doi.org/10.1021/acssuschemeng.6c04002
ACS Sustain. Chem. Eng. 2026, 14, 14720−14732

sequential compression, dragging, and detachment on the PSS. The θ_{WSA} of the PSS was measured using a Digital Angle Finder (GAM 2220 MF, Bosch). The sample was mounted on the fold-out leg of the device with the base leg positioned horizontally. The tilt angle was gradually adjusted until a 10 μL droplet began to roll off the PSS surface, at which point the measurement was halted and θ_{WSA} was recorded.

PSS Abrasive Test

PSS's durability was evaluated by contacting the PSS surface with an abrasive paper, subjected to a load of 200 g applied perpendicularly to the surface. The assembly was then linearly drawn over the abrasive paper back and forth for different distances (0, 40, 80, 120, 160, and 200 cm). The modified PSS was evaluated using a Contact Angle Meter and a Digital Angle Finder to quantify θ_{WCA} and θ_{WSA}, assessing the influence of surface roughening on superhydrophobic performance.

Self-Cleaning Test

The self-cleaning performance of the SP-derived PSS was assessed by depositing water onto a tilted PSS substrate (approximately 10°) with river sand particles serving as a solid contaminant. Both SP-PDMS and SP-PDMS-FTS PSS samples were evaluated by qualitatively evaluating the residual impurities remaining on the surfaces. The entire process was documented using a mobile phone camera.

RESULTS AND DISCUSSION

Pollen Superhydrophobic Surface (PSS) Fabrication

PSS was categorized into two components: the pollen-PDMS composite (PP) and the pollen-PDMS-FTS (PPF) composite. PSS is prepared by dispersing spiky pollen particles with low-surface-energy materials, either PP or a PPF blend, with *n*-hexane followed by drop-casting the mixture onto a substrate. Following solvent evaporation, the deposited layer was left to cure to achieve full crosslinking and the formation of a superhydrophobic surface[39] (Figure 1a). To delineate whether superhydrophobicity could be driven predominantly via the spiky pollen architecture rather than fluorinated modifications, the role of spiky pollen's geometrical features was examined. For this purpose, four spiky pollen species were selected: ragweed, chrysanthemum subspecies 1 (C1), chrysanthemum subspecies 2 (C2), and sunflower. These species exhibit size monodispersity and predominantly spheroidal geometries, displaying slight variations in pollen size but more pronounced differences in spike length (L) (Figure 1b). These pollen species

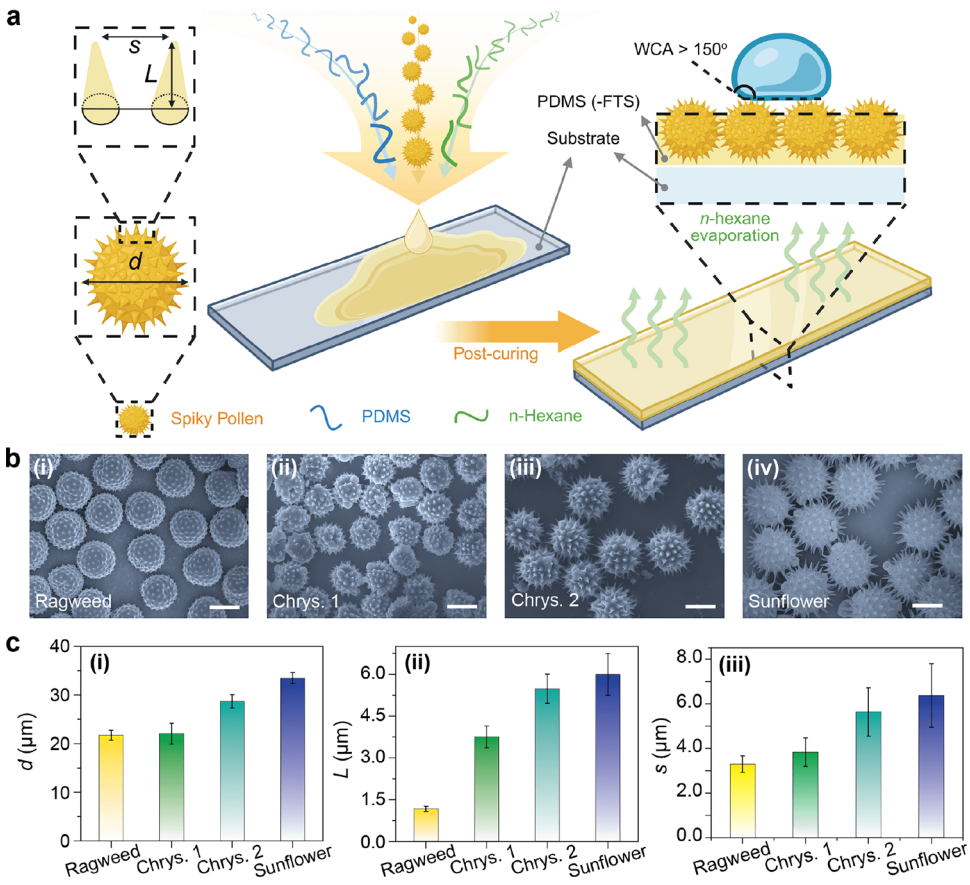

Figure 1. Pollen superhydrophobic surface (PSS) formation utilizing different spiky pollen particles. (a) Schematic for PSS fabrication and its resultant configuration. The precursor consisting of defatted spiky pollen, polydimethylsiloxane (PDMS), 1*H*,1*H*,2*H*,2*H*-perfluorooctyl-trichlorosilane (FTS), and *n*-hexane is drop-cast onto a glass substrate forming the PSS after *n*-hexane evaporation and PDMS curing, PSS fabrication is differentiated into two components: (1) pollen-PDMS (PP) composites are fluorine-free, whereas (2) pollen-PDMS-FTS (PPF) composites are fluorine-modified. (b) SEM images of various spiky pollen particles including (i) ragweed, (ii) chrysanthemum subspecies 1 (Chrys. 1), (iii) chrysanthemum subspecies 2 (Chrys. 2), and (iv) sunflower exhibiting unique and uniform morphologies, Scale bar = 20 μm. (c) Variations in spiky pollen morphologies differing in (i) pollen size (d), (ii) spike length (L), and (iii) interspike spacing (s).

https://doi.org/10.1021/acssuschemeng.6c04002
ACS Sustain. Chem. Eng. 2026, 14, 14720−14732

exhibit average sizes (d) of 21.7, 22.0, 28.7, and 33.5 μm with spike lengths measuring 1.2, 3.8, 5.5, and 6.0 μm and interspike spacings (s) of 3.3, 3.8, 5.6, and 6.4 μm, respectively (Figure 1c).

PSS's Superhydrophobic Performance

To replicate the conical micro/nanostructured surface exhibited on lotus leaves,[18−20] the influence of the mass fraction of pollen (f_{pollen}) on achieving pollen-derived surface topographies was systematically examined. SEM characterization at different f_{pollen} values (30−70%) was performed for the selected spiky pollen species (Figure 2a). At f_{pollen} = 30%, most pollen grains were embedded within the PDMS matrix. Notably, ragweed and Chrys. 2 revealed a partial protrusion of their cone-shaped nanostructures despite the retention of their bulk microstructure within the matrix. Beyond f_{pollen} = 40%, all pollen species except

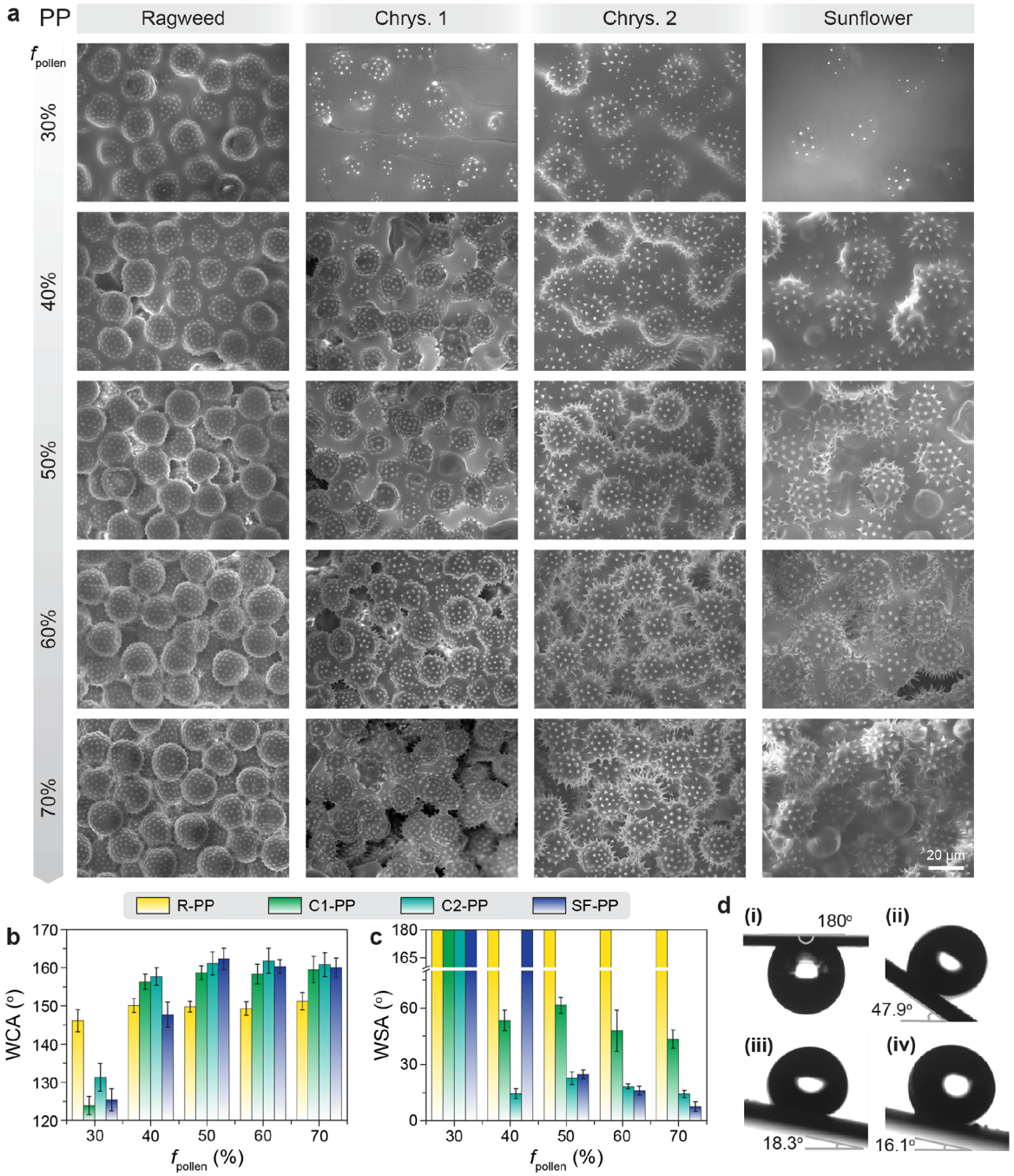

Figure 2. Various PSSs and their hydrophobicity characterization. (a) SEM images of the various pollen-PDMS (PP) surfaces with the mass fraction of pollen (f_{pollen}) from 30 to 70%. (b) Water contact angle (θ_{WCA})−f_{pollen} column plot showing that, at a low f_{pollen} of 30%, ragweed-PP (R-PP) exhibits near-superhydrophobicity, with other PP composites exhibiting superhydrophobicity past f_{pollen} = 50%. (c) θ_{WSA}−f_{pollen} column plot showing an overall decrease in water sliding angle (θ_{WSA}) as f_{pollen} increases, except for R-PP that remains constant throughout. (d) Images of θ_{WSA} for PP composites with f_{pollen} = 60%: (i) R-PP with θ_{WSA} of 180°, (ii) Chrys. 1-PP (C1-PP) with θ_{WSA} of 47.9°, (iii) Chrys. 2-PP (C2-PP) with θ_{WSA} of 18.3°, and (iv) sunflower-PP (SF-PP) with θ_{WSA} of 16.1°.

https://doi.org/10.1021/acssuschemeng.6c04002
ACS Sustain. Chem. Eng. 2026, 14, 14720−14732

sunflower exhibited discernible exposure of their microstructure while still being partially embedded within the matrix. In contrast, sunflower pollen required a higher threshold with pronounced microstructure exposure and partial encapsulation when f_{pollen} exceeds 50%. The variation in f_{pollen} threshold at which the pollen microstructure becomes discernible is attributed to their particle size. Larger pollen grains, such as those of sunflower, possess higher mass resulting in a smaller quantity for a given mass fraction. Conversely, smaller pollen grains such as ragweed present themselves in higher amounts at the same mass fraction. This disparity in pollen quantity leads to the same discernible pollen microstructure exposure at different f_{pollen} values.

To delineate the influence of different f_{pollen} values on superhydrophobic performance, θ_{WCA} and θ_{WSA} were evaluated across the entire f_{pollen} range to identify the ideal pollen loading (Figure 2b,c). Species-specific wetting behaviors were prominent across all PP composites. Ragweed-PP (R-PP) exhibited stable near-superhydrophobicity across all tested f_{pollen} values, with θ_{WCA} values ranging from 146° up to 151°. Furthermore, R-PP demonstrates near-superhydrophobicity even at f_{pollen} = 30%, which is consistent with its pronounced nanostructural exposure at low loading (Figure 2a). Both chrysanthemum pollen composites (C1-PP and C2-PP) achieved superhydrophobic levels beyond f_{pollen} = 40% with θ_{WCA} values of 156° and 158°, respectively. In contrast, sunflower composites (SF-PP) required a higher f_{pollen} content, achieving near-superhydrophobicity at 40% and attaining superhydrophobicity beyond 50% with θ_{WCA} values of 148° and 162°, respectively. Almost all the pollen composites reach their peak θ_{WCA} at f_{pollen} = 50%, except for C2-PP that peaked at f_{pollen} = 60% before experiencing a slight decline in θ_{WCA}. θ_{WSA} was further assessed against f_{pollen} to quantify the influence of spiky pollen on superhydrophobic performance (Figure 2c,d). However, the variations in θ_{WSA} were not solely dependent on f_{pollen}, as most pollen species exhibit decreased θ_{WSA} with increasing f_{pollen} except for ragweed. R-PP consistently maintained θ_{WSA} of 180° across all f_{pollen} content, with the droplet adhering to the surface despite being inverted, characteristics of the "petal effect" (Figure 2d−i).[21−23] To further quantify the dynamic wetting performance of PP, θ_{CAH} was assessed with f_{pollen} = 60%, selected as an optimal loading that balances the slight decrease in θ_{WCA} observed above f_{pollen} = 50% with the continuous reduction in θ_{WSA}. At f_{pollen} = 50%, θ_{WCA} values are 150°, 159°, 161°, and 162° for R-PP, C1-PP, C2-PP, and SF-PP, respectively, whereas at f_{pollen} = 60%, the corresponding θ_{WCA} values are 149°, 158°, 162°, and 160° (Figure S1). The f_{pollen} = 60% PP recorded θ_{CAH} values of 44.3°, 17.1°, 11.1°, and 13.5°, respectively, with only the R-PP exhibiting moderately high θ_{CAH} while maintaining superhydrophobicity (Figure S2a. In contrast, the other PPs achieved θ_{CAH} values close to those theoretically expected for an ideal superhydrophobic surface (<10°).[12,13] R-PP exhibited an extremely elevated θ_{CAH} despite maintaining a high θ_{WCA}, a characteristic of the "petal effect" or the representation of the CI wetting state.[13,43]

To support the superhydrophobic behavior, the surface roughness ratio (r) and solid−liquid contact fraction (f_1) were evaluated using the Wenzel and CB models, respectively (all equations and calculations derived are provided in Figure S3). Based on the Wenzel model, r reflects the ratio between the actual rough surface area and the ideal smooth surface, with $r > 1$ indicating a rough surface.[44] At f_{pollen} = 60%, C1-PP exhibits the highest r (1.405) followed by C2-PP (1.296), SF-PP (1.271), and R-PP (1.127), confirming that all PP composites possess rough surfaces (Figure S4). Using the CB model, f_1 was evaluated where when f_1 approaches 0, it indicates a superhydrophobic state (θ_{WCA} = 180°), while f_1 = 1 corresponds to complete wetting.[44] At f_{pollen} = 60%, R-PP exhibits the highest f_1 (0.543) followed by C1-PP (0.031), C2-PP (0.019), and SF-PP (0.014) (Figure S5). These results are consistent with the θ_{WCA} observed and provide insight into the influence of variations in different spiky pollen geometrical features on superhydrophobicity.

To evaluate whether fluorinated modifications are necessary to achieve superhydrophobic performance or whether the spiky pollen architecture is sufficient, FTS was introduced into the PDMS matrix to further reduce surface free energy. A PPF composite of composition f_{pollen} = 60%, 30 wt % PDMS, and 10 wt % FTS was prepared. FTS incorporation yields a slight incremental improvement across all superhydrophobic metrics. θ_{WCA} increased across all species spanning from 153° to 169°, while θ_{WSA} decreased to 44.7°, 9.1°, and 6.8° for C1-PPF, C2-PPF, and SF-PPF, respectively (Figure S2b,c). θ_{CAH} values of 30.2°, 13.6°, 12.7°, and 7.8° were recorded for R-PPF, C1-PPF, C2-PPF, and SF-PPF, respectively, with SF-PPF approaching the superhydrophobic characteristics of a lotus leaf (Figure S2d).[16] R-PPF, however, remained with a θ_{WSA} of 180° while retaining a moderately high θ_{CAH}, confirming the persistence of the CI wetting state regardless of surface energy reduction (Figure S2c,d). While the incorporation of FTS conferred an enhancement in PPF's superhydrophobic properties, fluorine-free PP composites achieved a comparable low-adhesive superhydrophobic performance with a reduced environmental burden.[17]

To further clarify that the observed superhydrophobicity arises from a cooperative effect between the spiky pollen architectures and the low-energy matrix (PDMS and PDMS_FTS), θ_{WCA} was measured for both bare SF pollen and PDMS and compared against their corresponding SF-PP and SF-PPF composites. X-ray photoelectron spectroscopy (XPS) was first employed to verify the stepwise surface modification from bare sunflower pollen to PP and PPF. Compared with defatted pollen, PP exhibits distinct Si 2s and Si 2p signals at 151.5 and 102 eV, respectively, confirming the successful deposition of PDMS on the pollen surface. After FTS incorporation, PPF further displayed a characteristic F 1s signal at 684.8 eV and fluorocarbon-related C 1s components assigned to C−F_2 and C−F_3 bonds, verifying the introduction of fluorinated groups onto the PDMS-coated pollen surface (Figure S6). Bare SF displays an average θ_{WCA} of 103°, while PDMS alone exhibits an average θ_{WCA} of 118°, indicating that neither component independently exhibits a superhydrophobic behavior (Figure S7). In contrast, combining SF pollen with PDMS (SF-PP) increases θ_{WCA} to 160°, and further incorporation of FTS (SF-PPF) elevates θ_{WCA} to 169°. This stepwise enhancement shed insight into the superhydrophobic behavior arising from the interplay between the pollen architecture and the low-surface-energy matrix rather than the intrinsic wettability of pollen or PDMS alone. From a geometrical perspective, superhydrophobic properties increased systematically with increasing spike length from 1.2 to 6.0 μm. θ_{WCA} increased progressively with spike length for both PP and PPF composites, with the PPF composite yielding higher θ_{WCA} values than PP across the entire range investigated (Figure 3a). The influence of spike length on θ_{WSA} was considerably more pronounced, with a stark decline observed in θ_{WSA} value as spike length increased (Figure 3b). θ_{CAH} experiences an analogous decreasing trend with increasing spike length (Figure 3c), collectively indicating the

https://doi.org/10.1021/acssuschemeng.6c04002
ACS Sustain. Chem. Eng. 2026, 14, 14720−14732

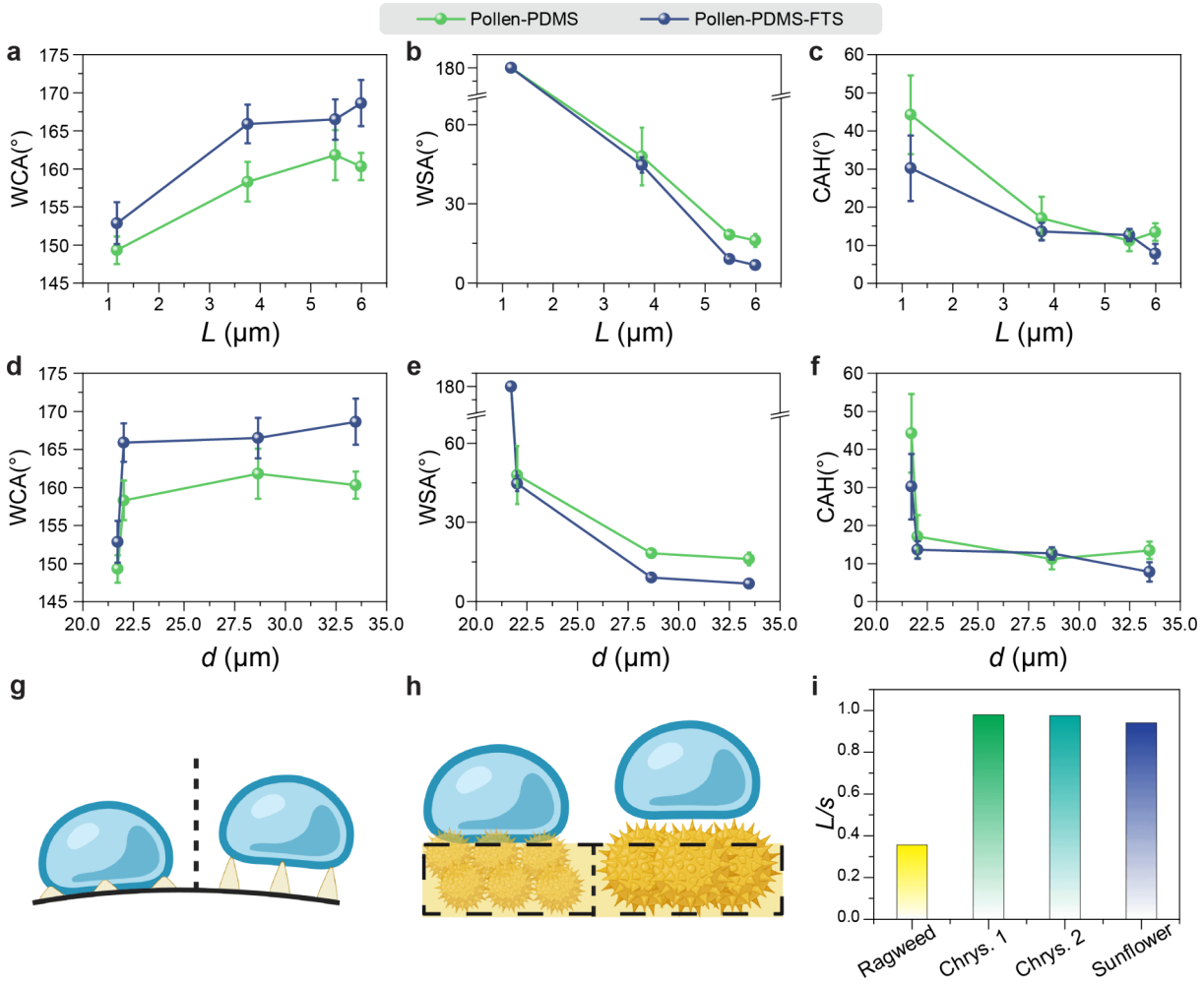

Figure 3. Influence of pollen's geometrical features on superhydrophobic properties of PSS (f_{pollen} = 60%). Effect of spiky pollen's L on PSS's superhydrophobic performance: (a) θ_{WCA}, (b) θ_{WSA}, and (c) contact angle hysteresis (θ_{CAH}). Effect of spiky pollen's d on PSS's superhydrophobic performance: (d) θ_{WCA}, (e) θ_{WSA}, and (f) θ_{CAH}. Schematic representation of spiky pollen's geometrical features on superhydrophobicity: (g) influence of L and (h) influence of d. (i) Spike length over interspike spacing (L/s) column plot.

positive influence of longer spikes on superhydrophobic metrics. This trait is attributed to the spiky pollen's inherent geometric architecture influence on surface roughness and wetting state (Figure 3g).

In contrast to spike length, pollen size exerted a comparatively weaker influence on wetting behavior (Figure 3d–f). A steep improvement in superhydrophobic metrics was observed when pollen size slightly increased from 21.7 to 22.0 μm, beyond which both θ_{WCA} and θ_{CAH} exhibited relatively stable values with only minor fluctuations. θ_{WSA} followed a two-stage decline: a steep reduction from 21.7 to 22.0 μm followed by a more gradual decrease from 22.0 to 28.7 μm before plateauing at larger sizes. Consistent with the spike length trends, PPF composites demonstrate superior θ_{WCA} and θ_{WSA} relative to their PP counterparts. This weaker size dependency suggests that pollen size influences superhydrophobic performance indirectly, principally by governing the extent of spike protrusion above the PDMS matrix (Figure 3h), whereas spike length remains a dominant geometric feature directly modulating surface roughness and influencing wetting behavior (Figure 2a).

Critically, pollen species possessing shorter spike length present lower surface roughness and the generation of larger microgrooves between spikes, facilitating liquid impregnation and inducing a transition to the CI state.[45,46] However, when comparing s with superhydrophobic properties, a smaller s is associated with poorer superhydrophobicity, whereas a larger s corresponds to enhanced superhydrophobicity for both PP and PPF composites (Figure S8). To capture the combined effect of L and s, a spike length to interspike spacing (L/s) parameter was proposed as a simple geometric descriptor of the effectiveness of pollen spikes in supporting a water droplet (Figure 3i). A higher L/s denotes spikes that are more pronounced relative to their spacing (longer L and/or closer packing) reducing the effective solid-liquid contact area favoring the CB wetting state. Importantly, although larger microgrooves generally facilitate liquid penetration promoting the CI wetting state, the overall wetting behavior of pollen is governed by a holistic interplay of geometrical features with L exerting a more dominant influence than d and s (Figure S9).

Droplet Impact and Adhering Tests on PSSs

To further evaluate the superhydrophobic properties of the PSS, the droplet impact and adhering behavior were evaluated. Droplet impact on PSS was assessed by releasing a 6 μL water

https://doi.org/10.1021/acssuschemeng.6c04002
ACS Sustain. Chem. Eng. 2026, 14, 14720–14732

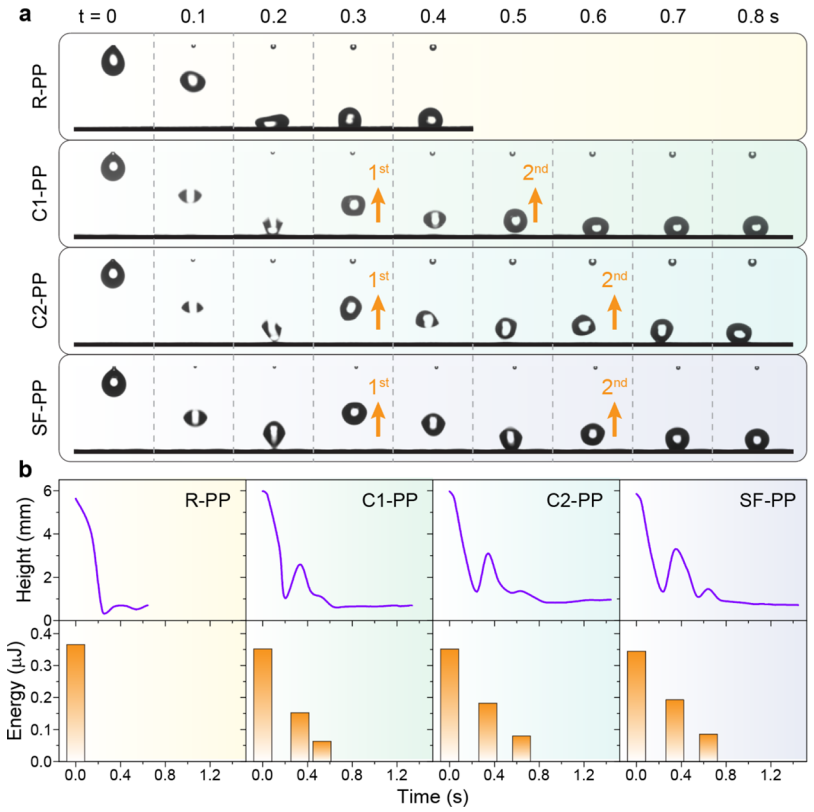

Figure 4. PP composites' (f_{pollen} = 60%) water adhesion characterization. (a) Bounce test results for PP composites (including R-PP, C1-PP, C2-PP, and SF-PP). The test evaluates PP's adhesion performance by quantifying the occurrence of water droplet bouncing. The arrows denote the droplet's direction after rebounding from the substrate. (b) Height−time curve and the corresponding rebound energy distributions for a droplet impacting PP composites.

droplet from a height of 6 mm onto different PP composites, and its impact behavior was recorded from 0 to 0.8 s (Figure 4a). R-PP displayed an adhesive response, with the droplet experiencing a brief compression around 0.2 s and remaining immobilized on the surface with no detectable rebound, indicating pronounced droplet pinning. This pinning state resembles the "petal effect" or CI wetting state in which the droplet's base is effectively immobilized on the R-PP surface.[21−23] In addition, the hydrophobicity evaluation of R-PP further supports the demonstration of the "petal effect" with a high θ_{WCA} (149°), θ_{WSA} (180°), and θ_{CAH} (44.3°) (Figure 2b,c and Figure S2a).[47] In contrast, the other PP composites demonstrated varying degrees of water repellence, with the other composites exhibiting two rebounds. The second rebound on C1-PP is hardly discernible at around 0.5 s when compared to both C2-PP and SF-PP surfaces, which undergo a second rebound visibly at around 0.6 s. The multiple bounce behavior suggests that for the longer spike length, the composites could effectively trap air within the pollen rough micro/nanostructures, exhibiting the "lotus effect" or CB wetting state (Figure 3a−c).[18,45,46] The hydrophobicity evaluation of C2-PP and SF-PP further supports the "lotus effect" phenomenon with a high θ_{WCA} (162° and 160°, respectively) and low θ_{WSA} (18.3° and 16.1°, respectively) and θ_{CAH} (11.1° and 13.6°, respectively) (Figure 2a,b and Figure S2a). However, C1-PP, despite demonstrating superhydrophobic θ_{WCA} of 158°, has a relatively higher θ_{WSA} of 47.9° and slightly enhanced θ_{CAH} of 17.1° compared to C2-PP and SF-PP, leading to a faster second and hardly discernible bounce at 0.5 s (Figure 2a,b and Figure S2a).

To further distinguish the impact dynamics among the PP composites, a height−time and rebound energy analysis was performed (Figure 4b). Based solely on the bounce observations, both C2-PP and SF-PP appeared to suppress droplet adhesion more effectively than the rest, but their individual performance could not be clearly differentiated. The height−time profiles and corresponding rebound energy distributions provided a clearer assessment of the suppression of adhesion. All composites exhibited comparable initial rebound energies in the range of 0.332−0.352 μJ, confirming that the initial impact and energy transfer were similar across composites. In contrast, differences became pronounced in subsequent rebounds with C1-PP, C2-PP, and SF-PP, illustrating first rebound energies of 0.152, 0.182, and 0.193 μJ and second rebound energies of 0.063, 0.080, and 0.086 μJ, respectively. The higher retained rebound energies and contact time for C2-PP and SF-PP indicate a reduction in the rebound energies due to the enhanced capabilities of the composites to suppress adhesion leading to more efficient droplet detachment. The enhanced resilience to rebound energy is attributed to its longer spike features, effectively trapping air within the microstructured features and promoting the CB wetting state.

Subsequently, to complement the droplet impact measurements, an adhesion test was conducted to directly probe the droplet−surface interaction under compression, lateral sliding, and separation (Figure 5). The results reinforced the PP

https://doi.org/10.1021/acssuschemeng.6c04002
ACS Sustain. Chem. Eng. 2026, 14, 14720−14732

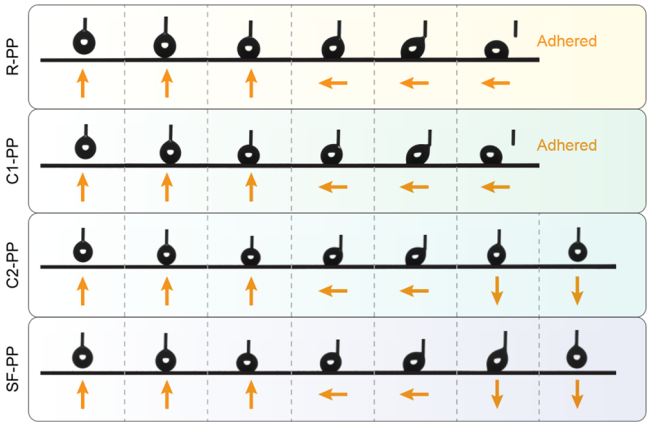

Figure 5. Adhesion test for PP composites to determine adhesion behavior by analyzing the occurrence of droplet adhesion. The arrows denote the direction of the substrate movement.

composites' superhydrophobic performance, with R-PP exhibiting a strong CI wetting response and retaining the droplet to the composite, confirming its highly adhesive CI wetting state. In contrast, despite C1-PP demonstrating two successive rebounds in the impact test, it still enabled noticeable droplet adhesion indicative of the intermediate wetting behavior of C1-PP due to the intrinsic pollen topography of C1 that features an intermediate spike length between R-PP and C2-PP (Figure 1c-ii), thereby providing only partial air entrapment and a slightly less robust CB state. By comparison, C2-PP and SF-PP effectively suppress droplet adhesion, in line with their impact dynamics (Figure 4) and superhydrophobic behavior (Figure 2b–d and Figure S2a,b) that typify the CB wetting state.

Postmodification with FTS further enhanced the water repellency of all PP composites, promoting rebound and suppressing droplet adhesion across the PPF composites (Figure 6). Notably, R-PPF only demonstrated a weak, single rebound at 0.24 s before droplet immobilization (Figure 6a), whereas C1-PPF retained the two-rebound behavior of its PP counterparts,

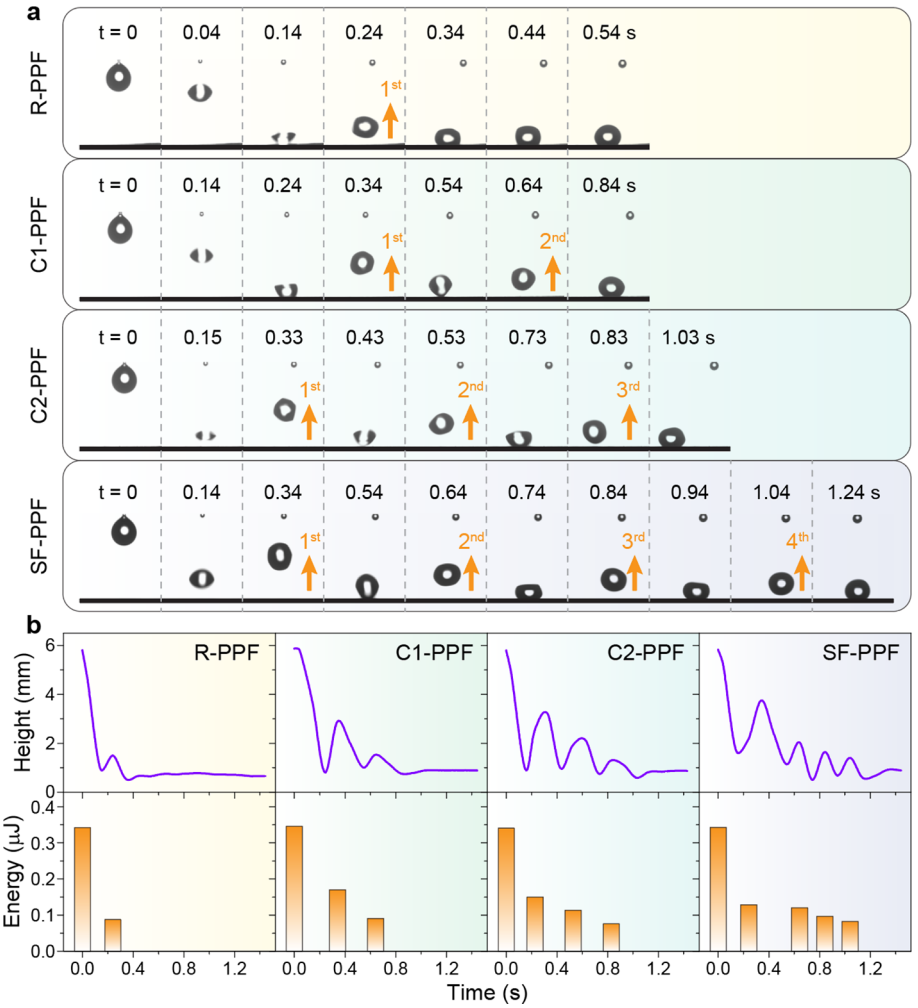

Figure 6. PPF composites (f_{pollen} = 60%) water adhesion characterization. (a) Bounce test results for PPF composites (including ragweed-PPF (R-PPF), Chrys. 1-PPF (C1-PPF), Chrys. 2-PP (C2-PPF), and sunflower-PPF (SF-PPF)). The test evaluates PPF's adhesion performance by quantifying the occurrence of water droplet bouncing. The arrows denote the droplet's direction after rebounding from the substrate. (b) Height–time curve and the corresponding rebound energy distributions for a droplet impacting PPF composites.

https://doi.org/10.1021/acssuschemeng.6c04002
ACS Sustain. Chem. Eng. 2026, 14, 14720–14732

with two successive rebounds at 0.34 and 0.64 s. In contrast, C2-PPF and SF-PPF exhibit marked improvements in their impact dynamics, with C2-PPF achieving three distinct rebounds at 0.33, 0.53, and 0.83 s and SF-PPF sustaining four successive rebounds at 0.34, 0.64, 0.84, and 1.04 s.

The corresponding height−time and rebound analysis provides quantitative behavior (Figure 6b). All PPF composites exhibited similar initial rebound energy in the range of 0.342−0.345 μJ, indicating comparable impact conditions. Despite supporting only one rebound, R-PPF demonstrated a roughly 4-fold reduction in rebound energy from 0.342 to 0.083 μJ, underscoring the limited ability of the short spikes to sustain repeated elastic rebounds. For C1, PPF modification modestly increased the energy from 0.152 to 0.170 μJ for the first rebound and 0.063 to 0.090 μJ for the second rebound but did not alter the total number of rebounds, highlighting that spike lengths exert a stronger influence on rebound dynamics than the surface chemistry alone. More pronounced changes are observed for C2 and SF-PPF in both their cumulative rebounds and rebound energetics. Relative to their PP counterparts, the height−time and rebound energy analysis suggests that both composites exhibit a lower rebound energy at the first rebound but a higher rebound energy at the second rebound. For C2, the first rebound energy decreases from 0.182 to 0.150 μJ upon FTS modification, while the second rebound energy increases from 0.080 to 0.113 μJ followed by a third rebound energy of 0.076 μJ. Similarly, SF-PPF demonstrated a larger drop in first rebound energy from 0.193 to 0.128 μJ, an increase in second rebound energy from 0.086 to 0.120 μJ, and a third and fourth rebound energies of 0.097 and 0.083 μJ, respectively. This nonmonotonic behavior of rebound energy could arise due to the Cassie-to-Wenzel wetting transition, which during early impacts incurs additional energetic cost and results in the modified rebound energies at the first and second rebound. After the initial restructuring, the droplet relaxes toward a CB state probably supported by the micro/nanostructured topographies of the spiky pollen so that subsequent rebounds occurred on a more robust air cushion, leading to more consistent, successive rebound energies.[48]

The adhesion test showed that, except for R-PPF, all PPF composites effectively suppressed droplet adhesion (Figure 7).

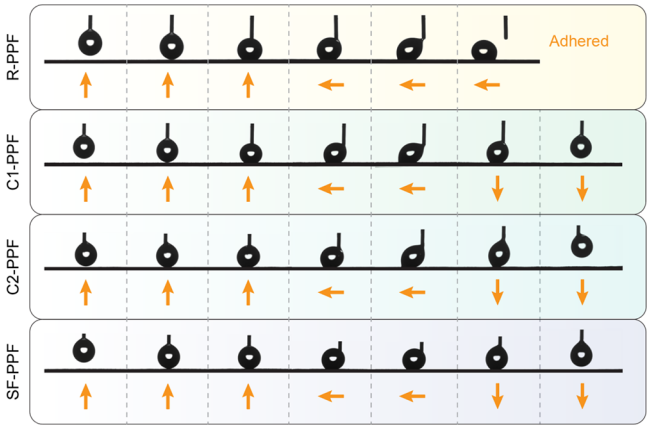

Figure 7. Adhesion test for PPF composites to determine adhesion behavior by analyzing the occurrence of droplet adhesion. The arrows denote the direction of the substrate movement.

R-PPF still exhibited a CI wetting response retaining the droplet despite FTS modification, although its superhydrophobic parameters shifted toward slightly enhanced hydrophobicity with an increased θ_{WCA} from 149° to 153° and a reduced θ_{CAH} from 44.3° to 30.2°, while θ_{WSA} remains unchanged. This combination of superhydrophobic-level θ_{WCA} with a large hysteresis explains the persistence of a strong droplet pinning behavior and observation of only a single rebound. Upon FTS modification, C1-PPF transitioned from an adhesive to a nonadhesive state, suppressing droplet adhesion during the adhesion test. This change is accompanied by an increase in θ_{WCA} from 158° to 166° and decreases in both θ_{WSA} (47.9° to 44.7°) and θ_{CAH} (17.1° to 13.6°). Similarly, C2- and SF-PPF preserved their nonadhesive behavior after modification. C2-PPF exhibited a higher θ_{WCA} (162° to 167°), a markedly lower θ_{WSA} (18.3° to 9.1°), and a slight increase in θ_{CAH} (11.1° to 12.7°), while SF-PPF exhibits an increasing θ_{WCA} from 160° to 169° and a decrease in both the θ_{WSA} (16.1° to 6.8°) and θ_{CAH} (13.6° to 7.8°). Collectively, the modifications from PP to PPF composites reveal that, while FTS modifications uniformly boost the superhydrophobic performance, it is the underlying pollen spike geometries particularly spike length that dictate the wetting transition of CI and CB states.

Durability and Self-Cleaning Properties of PSS

To evaluate the durability of the PSS, a sandpaper abrasion test was performed on the PP composites containing $f_{pollen} = 60\%$ (Figure 8a). Only PP composites were tested to isolate the contribution of the PP architecture to mechanical robustness without the added complexity of a fluorinated overlay that might mask structural impacts. The composites were abraded over progressive distances with both θ_{WCA} and θ_{WSA} recorded at each interval (Figure 8b). Following the abrasive test, all PP composites exhibited a fluctuation but an overall increase in θ_{WCA}, indicating that new roughened microstructures were induced while the low-energy PDMS matrix was retained. Concurrently, both C-PP composites experienced a decrease in their θ_{WSA} values, whereas R-PP remained nearly unchanged and SF-PP experienced a modest increase, confirming that the PP composites can withstand mechanical wear while largely preserving, and in some cases enhancing, the superhydrophobic properties.

The self-cleaning performance of the PSS was then assessed by depositing natural river sand onto both pristine PP and PPF composites followed by tilting and rinsing with water droplets (Figure 8c). Consistent with their higher adhesive behavior, R-PP surfaces trapped coagulated droplets and left residual contaminants along the surface. In contrast, C1- and C2-PP removed almost all the contaminants in the droplet pathway, with only a single droplet occasionally remaining, while SF-PP achieved complete contaminant removal without any droplet retention, reflecting effective self-cleaning capabilities. Similar trends were observed for the PPF composites, with nearly all PPF composites exhibiting self-cleaning capabilities except R-PPF, which still retained pinned water and a small fraction of residual contaminants. Taken together, these results suggest that even without FTS modification, the PP architecture can deliver robust superhydrophobicity with effective self-cleaning capabilities comparable to their PPF counterparts while completely avoiding the use of harmful, environmentally persistent fluorinated compounds.

https://doi.org/10.1021/acssuschemeng.6c04002
ACS Sustain. Chem. Eng. 2026, 14, 14720−14732

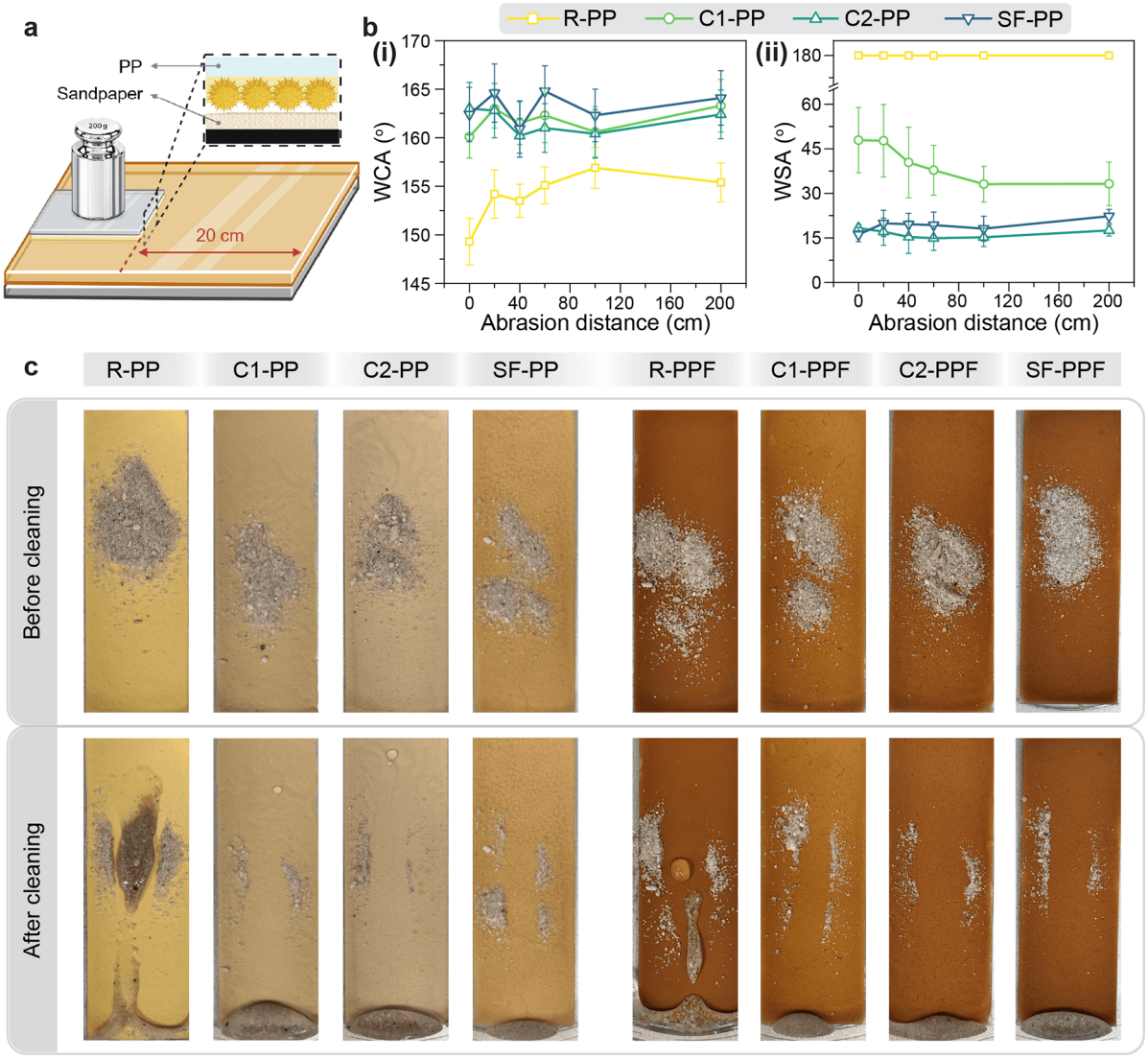

Figure 8. PSS's durability and self-cleaning characterization. (a) Schematic of the abrasive test where the PP composite (f_{pollen} = 60%) was pressed against abrasive paper under a 200 g load followed by progressive abrasion over increasing distance. (b) Superhydrophobic property indicators (i) θ_{WCA} and (ii) θ_{WSA} of PP composite against varying abrasion distance. (c) PSS self-cleaning performance (including PP and PPF composites).

Furthermore, the clearly distinctive change in wetting transition from R-PP to SF-PP due to different spike length could provide access to distinct CB and CI wetting response in SSs, broadening the accessible design space for functional wetting states. Such durable, pollen-inspired biomimetic surfaces therefore offer a fluorine-free platform for applications in self-cleaning buildings,[39] biomedical applications,[42] anti-icing surfaces,[41,49] and microfluidic droplet manipulation,[50] among others.

CONCLUSIONS

In this study, a range of spiky pollen species were systematically evaluated as natural templates for engineering and tuning of biomimetic superhydrophobic surfaces. Four distinctive species, including ragweed, wild chrysanthemum subspecies (C1 and C2), and sunflower, were investigated for their influence on superhydrophobicity and wetting behavior. The results demonstrate that the exceptional performance of PSS arises from the intrinsic spiky topographies of the pollen. Critically, the pollen's geometrical features play a major role in governing surface wettability and self-cleaning capability. Smaller pollen particles with shorter spikes, such as ragweed, exhibit near-superhydrophobicity (149° at 60% pollen) corresponding to the CI wetting state that involves strong droplet adhesion. In contrast, larger pollen particles with longer spikes, particularly sunflower, achieved outstanding water repellency and self-cleaning ability consistent with a CB wetting state. Upon fluorinated modification, all PP composites demonstrated enhanced superhydrophobicity. However, R-PPF retained its adhesive characteristics, underscoring that shorter spike topography governs a wetting state of CI even when surface chemistry is altered. Although fabrication methods of SS have advanced considerably, many either require extensive processing or are costly, are toxic, and/or risk secondary pollution.[51−56] In contrast, this study employs natural hydrophobic pollen to engineer tunable SSs via a facile drop-casting process, achieving comparable or superior superhydrophobic performance (Table S1). Remarkably, unmodified pollen composites alone exhibited excellent superhydrophobic properties, high robustness, and

https://doi.org/10.1021/acssuschemeng.6c04002
ACS Sustain. Chem. Eng. 2026, 14, 14720−14732

comparable self-cleaning capabilities to fluorinated counterparts but without their environmental drawbacks.

Beyond advancing sustainable material design, this study deepens the understanding of interfacial science by elucidating how the pollen's bioarchitecture governs the transition between wetting states and droplet adhesion, demonstrating its wide versatility and tunability. Furthermore, the sustainable and facile employment of spiky pollen as building blocks, arising from their intrinsic spiky architecture, represents a key advantage over conventional biobased or fluorine-free superhydrophobic systems that often rely on multistep processing to engineer surface roughness and low surface energy. Further exploration of pollen species with diverse topographies could expand the structure–wetting relationship to accelerate the development of the next generation of biobased superhydrophobic materials. More importantly, this approach exemplifies the essence of cross economy, transforming an abundant natural resource into a high-value material. By reimagining pollen "biowaste" as a versatile platform for advanced material innovation, this work transcends conventional circularity and paves the way toward a more resource-efficient future.

■ ASSOCIATED CONTENT

Supporting Information

The Supporting Information is available free of charge at https://pubs.acs.org/doi/10.1021/acssuschemeng.6c04002.

Contact angle images of PP composite; superhydrophobic property column plot of PP and PPF composites; schematics and theoretical calculation details; roughness ratio plot; solid–liquid contact fraction plot; contact angle measurements; XPS spectra; interspike spacing against superhydrophobic properties plot; schematic of the realistic interaction between pollen's geometrical features and superhydrophobic properties; and comparisons of various SSs with PSS (DOCX)

■ AUTHOR INFORMATION

Corresponding Author

Nam-Joon Cho – *School of Materials Science and Engineering, Nanyang Technological University, 639798 Singapore; Centre for Cross Economy, Nanyang Technological University, 637551 Singapore;* orcid.org/0000-0002-8692-8955; Email: NJCho@ntu.edu.sg

Authors

Jian Li – *School of Materials Science and Engineering, Nanyang Technological University, 639798 Singapore; Centre for Cross Economy, Nanyang Technological University, 637551 Singapore*

Chenchen Zhou – *School of Materials Science and Engineering, Nanyang Technological University, 639798 Singapore; Centre for Cross Economy, Nanyang Technological University, 637551 Singapore; State Key Laboratory of Micro-nano Engineering Science, School of Mechanical Engineering, Shanghai Jiao Tong University, Shanghai 200240, China*

Jun Hao Mo – *School of Materials Science and Engineering, Nanyang Technological University, 639798 Singapore; Centre for Cross Economy, Nanyang Technological University, 637551 Singapore*

Ruiyan Ni – *Shanghai Frontiers Science Center of Advanced Textiles, Donghua University, Shanghai 201620, China*

Jiwon Lee – *School of Materials Science and Engineering, Nanyang Technological University, 639798 Singapore; Centre for Cross Economy, Nanyang Technological University, 637551 Singapore*

Chee Hao Teo – *School of Materials Science and Engineering, Nanyang Technological University, 639798 Singapore; Centre for Cross Economy, Nanyang Technological University, 637551 Singapore*

Zi Hao Guo – *School of Electrical and Electronic Engineering, Nanyang Technological University, 639798 Singapore*

Hanna Kim – *School of Materials Science and Engineering, Nanyang Technological University, 639798 Singapore; Centre for Cross Economy, Nanyang Technological University, 637551 Singapore*

Mohammed Shahrudin bin Ibrahim – *School of Materials Science and Engineering, Nanyang Technological University, 639798 Singapore; Centre for Cross Economy, Nanyang Technological University, 637551 Singapore*

Bernard P. Binks – *Department of Chemistry, University of Hull, Hull HU6 7RX, U.K.;* orcid.org/0000-0003-3639-8041

Complete contact information is available at: https://pubs.acs.org/doi/10.1021/acssuschemeng.6c04002

Author Contributions

†J.Li, C.Z., and J.H.M. contributed equally to this work.
Jian Li and Chenchen Zhou conceived and designed this work under the supervision of Nam-Joon Cho. Jian Li, Chenchen Zhou, Jun Hao Mo, Mohammed Shahrudin Ibrahim, Jiwon Lee, Chee Hao Teo, Ruiyan Ni, and Hanna Kim performed the experiments. Jian Li, Chenchen Zhou, Jun Hao, Mohammed Shahrudin Ibrahim, Zihao Guo, and Nam-Joon Cho analyzed and discussed the experimental data. Chenchen Zhou, Jun Hao Mo, and Chee Hao Teo wrote and revised the paper with review and editing contributions from Bernard Binks and Nam-Joon Cho.

Notes

The authors declare that they have no known competing financial interests or personal relationships that could have appeared to influence the work reported in this paper.

■ ACKNOWLEDGMENTS

This study was supported by the Ministry of Education in Singapore under the MOE AcRF Tier 3 grant (Grant MOE-MOET32022-0002) as well as the Korea Health Technology R&D Project through the Korea Health Industry Development Institute (KHIDI), funded by the Ministry of Health & Wealth, Republic of Korea (Grant HI22C1394) and Ministry of Agriculture, Food, and Rural Affairs (Grant RS-2024-00403067). The TOC graphic; Figures 1a, 3g,h, and 8a; and Figures S3 and S9 were created with Biorender.com.

■ ABBREVIATIONS

SS	superhydrophobic surfaces
θ_{WCA}	water contact angle
θ_{WSA}	water sliding angle
θ_{CAH}	contact angle hysteresis

CB	Cassie−Baxter state
CI	Cassie-impregnating state
PDMS	Polydimethylsiloxane
PSS	pollen-based superhydrophobic surface
FTS	1*H*,1*H*,2*H*,2*H*-perfluorooctyl-trichlorosilane
PP	pollen-PDMS composite
PPF	pollen-PDMS-FTS composite
L	spike length
d	pollen's size
s	inter-spike spacing
f_{pollen}	mass fraction of pollen
R-PP/PPF	Ragweed-PP/PPF
C1-PP/PPF	Chrysanthemum subspecies1-PP/PPF
C2-PP/PPF	Chrysanthemum subspecies2-PP/PPF
SF-PP/PPF	Sunflower-PP/PPF
r	roughness ratio
f_1	solid-liquid contactfraction

REFERENCES

(1) Darmanin, T.; Guittard, F. Recent Advances in the Potential Applications of Bioinspired Superhydrophobic Materials. *J. Mater. Chem. A* **2014**, *2*, 16319−16359.

(2) Gao, X.; Yan, X.; Yao, X.; Xu, L.; Zhang, K.; Zhang, J.; Yang, B.; Jiang, L. The Dry-Style Antifogging Properties of Mosquito Compound Eyes and Artificial Analogues Prepared by Soft Lithography. *Adv. Mater.* **2007**, *19*, 2213−2217.

(3) Ma, M.; Hill, R. M. Superhydrophobic Surfaces. *Curr. Opin. Colloid Interface Sci.* **2006**, *11*, 193−202.

(4) Parvate, S.; Dixit, P.; Chattopadhyay, S. Superhydrophobic Surfaces: Insights from Theory and Experiment. *J. Phys. Chem. B* **2020**, *124*, 1323−1360.

(5) Wang, D.; Sun, Q.; Hokkanen, M. J.; Zhang, C.; Lin, F.-Y.; Liu, Q.; Zhu, S.-P.; Zhou, T.; Chang, Q.; He, B.; Zhou, Q.; Chen, L.; Wang, Z.; Ras, R. H. A.; Deng, X. Design of Robust Superhydrophobic Surfaces. *Nature* **2020**, *582*, 55−59.

(6) Brown, S.; Lengaigne, J.; Sharifi, N.; Pugh, M.; Moreau, C.; Dolatabadi, A.; Martinu, L.; Klemberg-Sapieha, J. E. Durability of Superhydrophobic Duplex Coating Systems for Aerospace Applications. *Surf. Coat. Technol.* **2020**, *401*, No. 126249.

(7) Falde, E. J.; Yohe, S. T.; Colson, Y. L.; Grinstaff, M. W. Superhydrophobic Materials for Biomedical Applications. *Biomaterials* **2016**, *104*, 87−103.

(8) Chen, H.; Cao, Y.; Wang, C.; Tie, F.; Dong, W.; Camaiti, M.; Baglioni, P. Superhydrophobic Surfaces for the Sustainable Maintenance of Building Materials and Stone-Built Heritage: The Challenges, Opportunities and Perspectives. *Adv. Colloid Interface Sci.* **2025**, *335*, No. 103343.

(9) Schmidt, D. L.; Brady, R. F.; Lam, K.; Schmidt, D. C.; Chaudhury, M. K. Contact Angle Hysteresis, Adhesion, and Marine Biofouling. *Langmuir* **2004**, *20*, 2830−2836.

(10) Yang, C.; Zeng, Q.; Huang, J.; Guo, Z. Droplet Manipulation on Superhydrophobic Surfaces Based on External Stimulation: A Review. *Adv. Colloid Interface Sci.* **2022**, *306*, No. 102724.

(11) Xiu, Y.; Zhu, L.; Hess, D. W.; Wong, C. P. Relationship between Work of Adhesion and Contact Angle Hysteresis on Superhydrophobic Surfaces. *J. Phys. Chem. C* **2008**, *112*, 11403−11407.

(12) Zaman Khan, M.; Militky, J.; Petru, M.; Tomková, B.; Ali, A.; Tören, E.; Perveen, S. Recent Advances in Superhydrophobic Surfaces for Practical Applications: A Review. *Eur. Polym. J.* **2022**, *178*, No. 111481.

(13) Ghosh, U. U.; Nair, S.; Das, A.; Mukherjee, R.; DasGupta, S. Replicating and Resolving Wetting and Adhesion Characteristics of a Rose Petal. *Colloids Surf. Physicochem. Eng. Asp.* **2019**, *561*, 9−17.

(14) Jiang, Y.; Choi, C.-H. Droplet Retention on Superhydrophobic Surfaces: A Critical Review. *Adv. Mater. Interfaces* **2021**, *8*, No. 2001205.

(15) Feng, L.; Li, S.; Li, Y.; Li, H.; Zhang, L.; Zhai, J.; Song, Y.; Liu, B.; Jiang, L.; Zhu, D. Super-Hydrophobic Surfaces: From Natural to Artificial. *Adv. Mater.* **2002**, *14*, 1857−1860.

(16) Wang, J. Lotus Leaf: Lotus Effect. In *Encyclopedia of Tribology*; Springer: Boston, **2013**, pp 2010−2016.

(17) Teisala, H.; Tuominen, M.; Aromaa, M.; Stepien, M.; Mäkelä, J. M.; Saarinen, J. J.; Toivakka, M.; Kuusipalo, J. Nanostructures Increase Water Droplet Adhesion on Hierarchically Rough Superhydrophobic Surfaces. *Langmuir* **2012**, *28*, 3138−3145.

(18) Zhang, M.; Feng, S.; Wang, L.; Zheng, Y. Lotus Effect in Wetting and Self-Cleaning. *Biotribology* **2016**, *5*, 31−43.

(19) Barthlott, W.; Neinhuis, C. Purity of the Sacred Lotus, or Escape from Contamination in Biological Surfaces. *Planta* **1997**, *202*, 1−8.

(20) Yamamoto, M.; Nishikawa, N.; Mayama, H.; Nonomura, Y.; Yokojima, S.; Nakamura, S.; Uchida, K. Theoretical Explanation of the Lotus Effect: Superhydrophobic Property Changes by Removal of Nanostructures from the Surface of a Lotus Leaf. *Langmuir* **2015**, *31*, 7355−7363.

(21) Feng, L.; Zhang, Y.; Xi, J.; Zhu, Y.; Wang, N.; Xia, F.; Jiang, L. Petal Effect: A Superhydrophobic State with High Adhesive Force. *Langmuir* **2008**, *24*, 4114−4119.

(22) Almonte, L.; Pimentel, C.; Rodríguez-Cañas, E.; Abad, J.; Fernández, V.; Colchero, J. Rose Petal Effect: A Subtle Combination of Nano-Scale Roughness and Chemical Variability. *Nano Sel.* **2022**, *3*, 977−989.

(23) Bormashenko, E.; Stein, T.; Pogreb, R.; Aurbach, D. "Petal Effect" on Surfaces Based on Lycopodium: High-Stick Surfaces Demonstrating High Apparent Contact Angles. *J. Phys. Chem. C* **2009**, *113*, 5568−5572.

(24) Bhushan, B.; Jung, Y. C. Natural and Biomimetic Artificial Surfaces for Superhydrophobicity, Self-Cleaning, Low Adhesion, and Drag Reduction. *Prog. Mater. Sci.* **2011**, *56*, 1−108.

(25) Liu, Z.; Zhang, C.; Jing, J.; Zhang, X.; Wang, C.; Liu, F.; Jiang, M.; Wang, H. Bristle Worm Inspired Ultra-Durable Superhydrophobic Coating with Repairable Microstructures and Anti-Corrosion/Scaling Properties. *Chem. Eng. J.* **2022**, *436*, No. 135273.

(26) Ke, C.; Zhang, C.; Wu, X.; Jiang, Y. Highly Transparent and Robust Superhydrophobic Coatings Fabricated via a Facile Sol-Gel Process. *Thin Solid Films* **2021**, *723*, No. 138583.

(27) Barthwal, S.; Barthwal, S.; Singh, B.; Bahadur Singh, N. Multifunctional and Fluorine-Free Superhydrophobic Composite Coating Based on PDMS Modified MWCNTs/ZnO with Self-Cleaning, Oil-Water Separation, and Flame Retardant Properties. *Colloids Surf., A* **2020**, *597*, No. 124776.

(28) Abeywardena, M. R.; Yashomala, M. A. D. H.; Elkaduwe, R. K. W. H. M. K.; Karunaratne, D. G. G. P.; Pitawala, H. M. T. G. A.; Rajapakse, R. M. G.; Manipura, A.; Mantilaka, M. M. M. G. P. G. Fabrication of Water-Repellent Polyester Textile via Dip-Coating of in-Situ Surface-Modified Superhydrophobic Calcium Carbonate from Dolomite. *Colloids Surf., A* **2021**, *629*, No. 127397.

(29) Goralczyk, A.; Savicheva, S.; Montazeri, R.; Fine, S.; Mayoussi, F.; Zhu, P.; Steffen, K.; Kotz-Helmer, F.; Helmer, D.; Rapp, B. E. Spray-Coating of Superhydrophobic Coatings for Advanced Applications. *Adv. Eng. Mater.* **2023**, *25*, No. 2201314.

(30) Celik, N.; Torun, I.; Ruzi, M.; Esidir, A.; Onses, M. S. Fabrication of Robust Superhydrophobic Surfaces by One-Step Spray Coating: Evaporation Driven Self-Assembly of Wax and Nanoparticles into Hierarchical Structures. *Chem. Eng. J.* **2020**, *396*, No. 125230.

(31) Raman, A.; Jayan, J. S.; Deeraj, B. D. S.; Saritha, A.; Joseph, K. Electrospun Nanofibers as Effective Superhydrophobic Surfaces: A Brief Review. *Surf. Interfaces* **2021**, *24*, No. 101140.

(32) Hardman, S. J.; Muhamad-Sarih, N.; Riggs, H. J.; Thompson, R. L.; Rigby, J.; Bergius, W. N. A.; Hutchings, L. R. Electrospinning Superhydrophobic Fibers Using Surface Segregating End-Functionalized Polymer Additives. *Macromolecules* **2011**, *44*, 6461−6470.

(33) Rezaei, S.; Manoucheri, I.; Moradian, R.; Pourabbas, B. One-Step Chemical Vapor Deposition and Modification of Silica Nanoparticles at

https://doi.org/10.1021/acssuschemeng.6c04002
ACS Sustain. Chem. Eng. 2026, 14, 14720−14732

the Lowest Possible Temperature and Superhydrophobic Surface Fabrication. *Chem. Eng. J.* **2014**, *252*, 11−16.
(34) Huang, X.; Sun, M.; Shi, X.; Shao, J.; Jin, M.; Liu, W.; Zhang, R.; Huang, S.; Ye, Y. Chemical Vapor Deposition of Transparent Superhydrophobic Anti-Icing Coatings with Tailored Polymer Nanoarray Architecture. *Chem. Eng. J.* **2023**, *454*, No. 139981.
(35) Li, L.; Wei, J.; Zhang, J.; Li, B.; Yang, Y.; Zhang, J. Challenges and Strategies for Commercialization and Widespread Practical Applications of Superhydrophobic Surfaces. *Sci. Adv.* **2023**, *9*, No. eadj1554.
(36) Zhou, C.; Deng, J.; Tay, J. H.; Basu, S.; Yang, J.; Li, J.; Yang, C.; Zhao, Z.; Cho, N. Multifunctional Material Building Blocks from Plant Pollen. *Annu. Rev. Chem. Biomol. Eng.* **2024**, *15*, 1−24.
(37) Fan, T.-F.; Park, S.; Shi, Q.; Zhang, X.; Liu, Q.; Song, Y.; Chin, H.; Ibrahim, M. S. B.; Mokrzecka, N.; Yang, Y.; Li, H.; Song, J.; Suresh, S.; Cho, N.-J. Transformation of Hard Pollen into Soft Matter. *Nat. Commun.* **2020**, *11*, 1449.
(38) Cho, N.-J. Preparing for Tomorrow with Materials Today. *Mater. Today* **2022**, *61*, 1−3.
(39) Li, J.; Deng, J.; Zhou, C.; Yang, J.; Shin, S.; Binks, B. P.; Cho, N.-J. Biomimetic Superhydrophobic Surfaces by Nanoarchitectonics with Natural Sunflower Pollen. *Small* **2025**, *21*, No. 2409136.
(40) Zhao, D.; Li, X.; Guo, Q.; Yang, Q.; Ye, C.; Shi, T.; Zheng, K.; Wang, Y. Recent Advances in Spiky Pollen-Inspired Functional Microparticles. *Appl. Mater. Today* **2023**, *35*, No. 101988.
(41) Dreischmeier, K.; Budke, C.; Wiehemeier, L.; Kottke, T.; Koop, T. Boreal Pollen Contain Ice-Nucleating as Well as Ice-Binding 'Antifreeze' Polysaccharides. *Sci. Rep.* **2017**, *7*, No. 41890.
(42) Ibrahim, M. S.; Ferhan, A. R.; Zhou, C.; Li, J.; Lin, Y.-C.; Deng, J.; Zhao, Z.; Cho, N.-J. Allergen to Asset: Pollen-Based Drug Delivery Systems. *Adv. Drug Deliv. Rev.* **2025**, *224*, No. 115643.
(43) Chakraborty, M.; Weibel, J. A.; Schaber, J. A.; Garimella, S. V. The Wetting State of Water on a Rose Petal. *Adv. Mater. Interfaces* **2019**, *6*, No. 1900652.
(44) Razavifar, M.; Abdi, A.; Nikooee, E.; Aghili, O.; Riazi, M. Quantifying the Impact of Surface Roughness on Contact Angle Dynamics under Varying Conditions. *Sci. Rep.* **2025**, *15*, 16611.
(45) Nyankson, E.; Agbe, H.; Takyi, G. K. S.; Bensah, Y. D.; Sarkar, D. K. Recent Advances in Nanostructured Superhydrophobic Surfaces: Fabrication and Long-Term Durability Challenges. *Curr. Opin. Chem. Eng.* **2022**, *36*, No. 100790.
(46) E, J.; Jin, Y.; Deng, Y.; Zuo, W.; Zhao, X.; Han, D.; Peng, Q.; Zhang, Z. Wetting Models and Working Mechanisms of Typical Surfaces Existing in Nature and Their Application on Superhydrophobic Surfaces: A Review. *Adv. Mater. Interfaces* **2018**, *5*, No. 1701052.
(47) Bami Chatenet, Y.; Valette, S. Elucidating the Lotus and Rose-Petal Effects on Hierarchical Surfaces: Study of the Effect of Topographical Scales on the Contact Angle Hysteresis. *J. Colloid Interface Sci.* **2024**, *676*, 355−367.
(48) Lee, C.; Nam, Y.; Lastakowski, H.; Hur, J. I.; Shin, S.; Biance, A.-L.; Pirat, C.; Kim, C.-J. "CJ."; Ybert, C. Two Types of Cassie-to-Wenzel Wetting Transitions on Superhydrophobic Surfaces during Drop Impact. *Soft Matter* **2015**, *11*, 4592−4599.
(49) Parra-Vicente, S.; Ibáñez-Ibáñez, P. F.; Cabrerizo-Vílchez, M.; Sánchez-Almazo, I.; Rodríguez-Valverde, M. Á.; Ruiz-Cabello, F. J. M. Understanding the Petal Effect: Wetting Properties and Surface Structure of Natural Rose Petals and Rose Petal-Derived Surfaces. *Colloids Surf., B* **2024**, *236*, No. 113832.
(50) Ebert, D.; Bhushan, B. Wear-Resistant Rose Petal-Effect Surfaces with Superhydrophobicity and High Droplet Adhesion Using Hydrophobic and Hydrophilic Nanoparticles. *J. Colloid Interface Sci.* **2012**, *384*, 182−188.
(51) Zhang, W.; Li, S.; Wei, D.; Zheng, Z.; Han, Z.; Liu, Y. Fluorine-Free, Robust and Self-Healing Superhydrophobic Surfaces with Anticorrosion and Antibacterial Performances. *J. Mater. Sci. Technol.* **2024**, *186*, 231−243.
(52) Liu, S.; Zhu, Z.; Zheng, Q.; Wang, K.; Zhou, F.; Yang, Q.; Wang, X.; Ye, L.; Chen, Y.; Liu, H.; Li, H. Waxberry-Liked Micro-Nanostructured, Superhydrophobic Surfaces with Enhanced Photothermal de-Icing and Passive Anti-Icing Properties. *Chem. Eng. J.* **2025**, *503*, No. 158358.
(53) Song, J.; Parker, R. M.; Frka-Petesic, B.; Deng, T.; Xu, L.; Deng, X.; Vignolini, S.; Shen, Q. Spray-Assisted Fabrication of Cellulose Photonic Pigments on Superhydrophobic Surfaces. *Adv. Mater.* **2025**, *37*, No. 2416607.
(54) Zhong, K.; Rozsa, J.; Patel, D. K.; Yao, L.; Fedder, G. K.; Islam, M. F. Aerosol Jet Printing of Superhydrophobic Surfaces. *Adv. Mater. Technol.* **2025**, *10*, No. 2401878.
(55) Zhang, C.; Pei, K.; Zhao, J.; Zhou, Y.; Zhang, S.; Han, X.; Guo, Z. Hierarchical Dandelion-like Superhydrophobic Surfaces with Excellent Stability and Photothermal Performance for Efficient Anti-/Deicing. *Chem. Eng. J.* **2025**, *510*, No. 161582.
(56) Huang, Z.; Zhu, S.; Zhu, M.; Tian, Y.; Ma, L. A Durable Superhydrophobic Surface with Bud-Particle Structure Prepared by One-Step Spray Method. *Appl. Surf. Sci.* **2025**, *679*, No. 161255.

https://doi.org/10.1021/acssuschemeng.6c04002
ACS Sustain. Chem. Eng. 2026, 14, 14720−14732